Genetic-algorithm-optimized wideband on-chip polarization rotator with an ultrasmall footprint

ZEJIE YU, HAORAN CUI, AND XIANKAI SUN*

Department of Electronic Engineering, The Chinese University of Hong Kong, Shatin, New Territories, Hong Kong
*Corresponding author: xksun@cuhk.edu.hk

Polarization control of light waves is an important technique in optical communication and signal processing. On-chip polarization rotation from the fundamental transverse-electric (TE_{00}) mode to the fundamental transverse-magnetic (TM_{00}) mode is usually difficult because of their large effective refractive index difference. Here, we demonstrate an on-chip wideband polarization rotator designed with a genetic algorithm to convert the TE_{00} mode into the TM_{00} mode within a footprint of $0.96\,\mu m \times 4.2\,\mu m$. In simulation, the optimized structure achieves polarization rotation with a minimum conversion loss of 0.7 dB and the 1-dB bandwidth of 157 nm. Experimentally, our fabricated devices have demonstrated the expected polarization rotation with a conversion loss of ~2.5 dB in the measured wavelength range of 1440–1580 nm, where the smallest value reaches ~2 dB. The devices can serve as a generic approach and standard module for controlling light polarization in integrated photonic circuitry.   © 2017 Optical Society of America

Silicon photonics based on the silicon-on-insulator (SOI) integrated platform has shown remarkable performance in wide applications, such as optical interconnects [1], optical modulation [2], nonlinear photonics [3], optomechanics [4], and biosensing [5], etc. Polarization control is an important technique in some applications, such as polarization-rotation-based modulation and switching [6,7]. However, the large effective refractive index contrast between the fundamental transverse-electric (TE_{00}) and transverse-magnetic (TM_{00}) modes not only makes it difficult to realize polarization-independent devices because of the polarization-dependent dispersion and loss [8–10], but also leads to substantial difficulty to achieve polarization rotation. To solve this problem, people have attempted many approaches with various designs, including triangular waveguides [11], asymmetric waveguides [12,13], waveguides with single or multiple etched trenches [14,15], waveguides with vertical and sloped sidewalls [16], coupling via an intermediate multi-mode waveguide [17], combination of horizontal and vertical waveguides [18], horizontal slot waveguides [19], adiabatic tapers [20], asymmetric directional couplers [21], cross-polarization-coupling directional couplers [22], waveguides using Berry's phase [23,24], and dual-core adiabatic tapers [25], etc. However, all these structures occupy a footprint of about tens of micrometers. In addition, the operating bandwidth of many of them is restricted to tens of nanometers.

Mathematical optimization is a general and robust design tool with wide applications in multidisciplinary areas of science and engineering [26]. Nanophotonic devices designed by mathematical optimization have achieved various functionalities, such as mode polarization splitter [27], wavelength (de)multiplexer [28,29], power splitter and divider [30,31], and multimode (de)multiplexer [32]. The optimized devices usually have the advantages of low loss, wideband, and ultrasmall footprint [33–35]. In this Letter, we demonstrate a mathematically optimized ultra-compact wideband on-chip TE_{00}-TM_{00} polarization rotator with low loss and high efficiency. We used a genetic algorithm for optimizing the device design, where the TE_{00}-TM_{00} mode conversion can be realized within an ultrasmall footprint of $0.96\,\mu m \times 4.2\,\mu m$. The simulated conversion loss and 1-dB bandwidth are 0.7 dB and 157 nm, respectively, with the extinction ratio higher than 15 dB in the wavelength range of 1450–1670 nm. Experimentally, our fabricated devices have achieved a conversion loss ~2.5 dB (smallest value ~2 dB) and an extinction ratio ~10 dB in the wavelength range of 1440–1580 nm.

The devices are designed on a SOI wafer with a 220-nm silicon device layer on 3-µm buried oxide. Since it is difficult to achieve direct TE_{00}-TM_{00} mode conversion with a high efficiency due to the large effective index difference, we introduced an intermediate mode TE_{10}, whose effective index sits between those of the TE_{00} and TM_{00} modes. We optimized first the TE_{00}-TE_{10} and TE_{10}-TM_{00} mode converters separately and then the combined structure.

To design the structure for mode conversion, we set the initial structures shown in Figs. 1(a) and 1(d) for the TE_{00}-TE_{10} and TE_{10}-TM_{00} mode conversion, respectively. The widths of the input and output waveguides are 500 nm. The structures are initially divided into two regions marked in gray and red. As shown in Fig. 1(g), the gray region denotes the etched area where a 40-nm-thick silicon layer remains on top of the oxide,
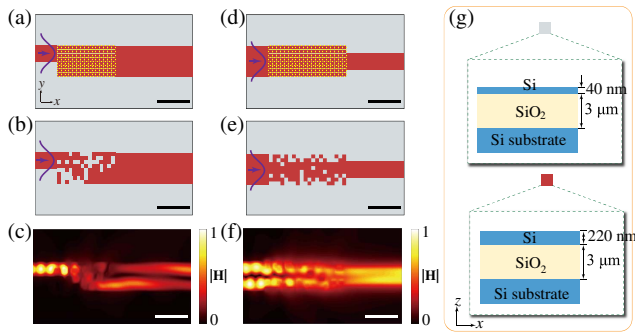
Fig. 1. (a, d) Initial structures for the TE$_{00}$-TE$_{10}$ (a) and TE$_{10}$-TM$_{00}$ (d) mode conversion. (b, e) Final optimized structures for the TE$_{00}$-TE$_{10}$ (b) and TE$_{10}$-TM$_{00}$ (e) mode conversion. (c) Field profile (|**H**| component) as the input TE$_{00}$ mode transmits from left to right through the structure in (b). (f) Field profile (|**H**| component) as the input TE$_{10}$ mode transmits from left to right through the structure in (e). (g) Color code for structures in (a, b, d, e). In (a)–(f), the operating wavelength is 1550 nm, and the scale bars represent 1 μm.

while the red region denotes the unetched area where the 220-nm silicon remains. For the etched area, we chose a 40-nm-thick remaining instead of a fully etched silicon layer mainly because the asymmetric structure along the z direction can contribute to the mode conversion and thus results in faster optimization speed. For optimizing the TE$_{00}$-TE$_{10}$ and TE$_{10}$-TM$_{00}$ conversion, we selected an area of 0.96 μm × 1.8 μm and 0.96 μm × 2.4 μm in the red region, consisting of 8 × 15 and 8 × 20 pixels as indicated by the yellow dashed grids in Figs. 1(a) and 1(d), respectively. Each pixel has a size of 120 × 120 nm^2, such that the rendered structure can faithfully be produced with the state-of-the-art nanofabrication techniques. The pixel size could influence the performance of device both in bandwidth and conversion efficiency, as discussed in [30]. We aimed to obtain high TE$_{00}$-TE$_{10}$ and TE$_{10}$-TM$_{00}$ mode conversion efficiencies by replacing some of the red pixels in the optimization area with a gray pixel. Figures 1(b) and 1(e) show the final optimized structures. Figures 1(c) and 1(f) show the field profiles (|**H**| component, wavelength 1550 nm) as the respective input mode transmits from left to right through the optimized structure.

The structural optimization was implemented with a genetic algorithm [36], which consists of the following steps: (i) randomly generating p initial populations as the first generation. Each population is an array of the device's pixel distribution, where "0" represents an etched pixel and "1" unetched. The array length is equal to the total number of pixels, and the array elements have one-to-one correspondence to the pixels. (ii) Evaluating each population's fitness, which is the TE$_{00}$-TE$_{10}$ or TE$_{10}$-TM$_{00}$ mode conversion efficiency at 1550 nm calculated in Lumerical with three-dimensional finite-difference time-domain simulation [37]. (iii) If the fitness is larger than 0.85 or does not increase for more than 15 generations, then the optimization process is stopped; otherwise, proceed to Step (iv). (iv) Producing new populations by selection, crossover, and mutation based on each population's fitness to update the current generation. In the selection and reproduction process, we used a roulette-wheel selection method [36] to select p populations as the new generation from the current generation. Each of the selected p populations has 70% probability to have a crossover with another population. During

crossover, the two parent populations are intermixed, as shown in Fig. 2(a), to generate two children populations to replace the parent populations, where the crossover point is randomly picked. After crossover, each population in the new generation has 10% probability of mutation where a random number of pixels are selected to flip. A loop is thus formed by going back to Step (ii) to evaluate the new generation followed by judgment in Step (iii) and population reproduction in Step (iv). We chose p for the TE$_{00}$-TE$_{10}$ and TE$_{10}$-TM$_{00}$ mode conversion to be 200 and 300, respectively. The progress of convergence is shown in Fig. 2(b). The process was stopped when the stop criterion was satisfied in Step (iii).

Next, we joined the above separately optimized structures and performed further optimization for achieving the TE$_{00}$-TM$_{00}$ mode conversion. Figure 3(a) shows the initial structure by joining the two optimized structures directly. The field profiles in Figs. 1(c) and 1(f) indicate imperfect conversion from the TE$_{00}$ to TE$_{10}$ mode and from the TE$_{10}$ to TM$_{00}$ mode, respectively. Therefore, we employed an additional optimization process to increase the TE$_{00}$-TM$_{00}$ mode conversion efficiency of the as-joined structure. We tested the results of individually flipping each of the 8 × 35 pixels in the combined optimization area in Fig. 3(a). For each change, we calculated the mode conversion efficiency and compared it with that of the previous configuration. The flip of a pixel was accepted only if a higher mode conversion efficiency was obtained. All the pixels were tested in series starting from the lower left one and ending at the top right one. The entire optimization process, including the previous designs for the separate TE$_{00}$-TE$_{10}$ and TE$_{10}$-TM$_{00}$ mode conversion and the additional optimization for the joined structure, took ∼96 h on a normal 8-core desktop computer. Figures 3(b) and 3(c) show, respectively, the final optimized structure of the TE$_{00}$-TM$_{00}$ mode converter and the corresponding field profile (|**H**| component) as the input TE$_{00}$ mode transmits through. Figures 3(d) and 3(e) are cross-sectional field profiles in the input and output waveguide, respectively, as indicated in Fig. 3(c). The blue solid lines in Fig. 3(f) plot the simulated spectra for the TE$_{00}$-TM$_{00}$ mode conversion and for the TE$_{00}$ mode transmission. The smallest TE$_{00}$-TM$_{00}$ mode conversion loss is 0.7 dB with the 1-dB bandwidth of 157 nm. The insertion loss for direct transmission of the TE$_{00}$ mode maintains higher than 15 dB in the wavelength range of 1450–1670 nm. The design robustness was also examined by simulating the individual effects of an overall etch depth offset of $\Delta h = \pm 10$ nm, corner smoothening with 40 nm rounded radius, and 10% etching lag, with the results shown in Fig. 3(g). The red dashed lines in Fig. 3(f) plot the simulated spectra of a modified structure with the above
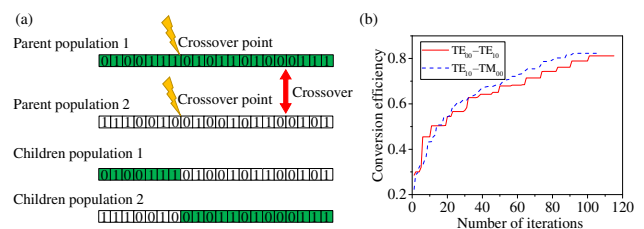

Fig. 2. (a) Illustration of crossover of two parent populations. (b) Convergence progress for optimizing the TE$_{00}$-TE$_{10}$ (red solid) and TE$_{10}$-TM$_{00}$ (blue dashed) mode conversion, respectively.
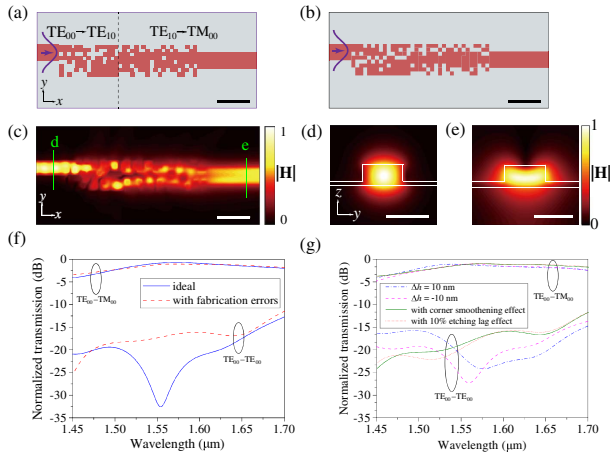
Fig. 3. (a, b) Initial (a) and final optimized (b) structure of the TE_{00}-TM_{00} mode converter. (c) Field profile ($|\mathbf{H}|$ component, wavelength 1550 nm) as the input TE_{00} mode transmits from left to right through the structure in (b). (d, e) Cross-sectional field profiles in the input (d) and output (e) waveguide as indicated in (c). (f) Simulated TE_{00}-TM_{00} mode conversion and TE_{00} mode transmission spectra for the ideal structure and for a modified structure with assumed fabrication errors. (g) Simulated spectra of structures with individual effects of an overall etch depth offset, rounded corners, and etching lag. The scale bars represent 1 μm in (a)–(c) and 0.5 μm in (d, e).

Fig. 4. (a, b) Optical microscope images of a TE_{00}-TM_{00} polarization rotator with TE-input, TM-output grating couplers (a) and with two TE grating couplers (b). (c) SEM image zoomed in at the TE_{00}-TM_{00} mode converter. (d, e) Optical microscope images of control devices, which consist of a pair of TE (d) or TM (e) grating couplers connected directly with a waveguide. (f) SEM image zoomed in at a TM grating coupler.

possible fabrication errors. It is clear that the optimized structure can work excellently as a wideband TE_{00}-TM_{00} mode converter.

We fabricated the TE_{00}-TM_{00} polarization rotator devices on a SOI wafer with a 220-nm Si device layer on 3-μm buried oxide. The patterns of the optimized TE_{00}-TM_{00} mode converter were defined along with the input and output waveguides in a single step of electron-beam lithography with ZEP520A resist. Then, the top silicon layer was etched to a depth of 180 nm by using inductively coupled plasma reactive ion etching. We also fabricated integrated grating couplers of targeted polarization on the chip for coupling the selected mode (TE_{00} or TM_{00}) of the waveguides into or out of an optical fiber. The etch depth of both the TE- and TM-type grating couplers is also 180 nm. The insertion loss of a single grating coupler is 7–10 dB. Because the TE- or TM-type grating couplers can act as optical polarizers with high extinction ratios of ~20 dB [38], we employed them for selecting the desired modal polarization in the input and output waveguides. Figures 4(a) and 4(b) are optical microscope images of a TE_{00}-TM_{00} polarization rotator with TE-input, TM-output grating couplers and with two TE-type grating couplers, respectively. Figure 4(c) is a scanning electron microscope (SEM) image zoomed in at the TE_{00}-TM_{00} mode converter, which has a footprint of only 0.96 μm × 4.2 μm. Control devices that consist of a pair of TE- or TM-type grating couplers connected directly with a rib waveguide [Figs. 4(d) and 4(e)] were also fabricated in the same run to calibrate the insertion loss introduced by the grating couplers. We fabricated multiple polarization rotator devices with grating couplers of different operating bands to overcome the limitation of narrower operating bandwidths of grating couplers.

The fabricated devices were characterized by spectroscopic measurement of their optical transmission. Light from a tunable
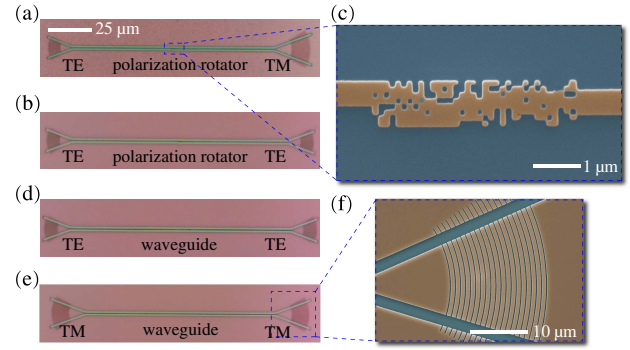
semiconductor laser (wavelength 1440–1580 nm) was sent over a single-mode fiber into the device via the input grating coupler, with the polarization state controlled by a fiber polarization controller. The transmitted light coupled out of the output grating coupler was collected by a photodetector. Figure 5 plots the normalized spectra for the TE_{00}-TM_{00} mode conversion and for the TE_{00} mode transmission, where the simulation for the fabricated structure was conducted by importing the device's SEM image into Lumerical and neglecting the roughness along the vertical (z) direction. The measured TE_{00}-TM_{00} mode conversion loss maintains at ~2.5 dB in the entire wavelength range, with the smallest value reaching ~2 dB. An average extinction ratio of 10 dB is identified with the measured TE_{00} mode transmission spectrum. These measurement results have clearly shown a high TE_{00}-TM_{00} mode conversion efficiency in a wide spectral range, which agrees well with the simulation results in Fig. 3(f). The slightly enhanced conversion loss and reduced extinction ratio compared with those of the simulated ideal structure are mainly caused by the uncontrollable imperfections during device nanofabrication, as confirmed by the simulated results of the fabricated structure in Fig. 5. Table 1 compares the experimental performance of our genetic-algorithm-optimized polarization rotator with other on-chip implementations. Our device achieves
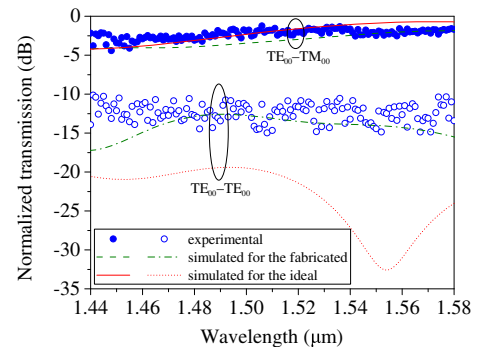

Fig. 5. Experimental and simulated normalized spectra for the TE_{00}-TM_{00} mode conversion and for the TE_{00} mode transmission.

Table 1. Comparison of On-Chip Polarization Rotators

References	Device Length (µm)	Conversion Loss (dB)	Extinction Ratio (dB)	1-dB Bandwidth (nm)
Velasco *et al.* [15]	10	0.7	16	<26
Liu *et al.* [22]	44	0.4	11	40
Aamer *et al.* [13]	25	0.85	5	<30
Zhang *et al.* [19]	100	1	14	>70
This work	4.2	2	10	~140

similar performance as the others within a length that is at least 2.4 times shorter.

In conclusion, we have designed and experimentally realized an ultracompact, wideband on-chip polarization rotator with a low conversion loss and high extinction ratio. The design relies on a genetic-algorithm optimization method that can be performed with a normal desktop computer. The device fabrication involves only a single step of electron-beam lithography with subsequent dry etching on a SOI wafer. With a footprint of only $0.96~\mu m \times 4.2~\mu m$, the fabricated devices have achieved the expected TE_{00}-TM_{00} polarization rotation, where the measured conversion loss is ~2.5 dB (smallest value ~2 dB) and the extinction ratio is ~10 dB in the wavelength range of 1440–1580 nm.

REFERENCES

1. D. Dai and J. E. Bowers, Nanophotonics **3**, 283 (2014).
2. Q. Xu, B. Schmidt, S. Pradhan, and M. Lipson, Nature **435**, 325 (2005).
3. J. Leuthold, C. Koos, and W. Freude, Nat. Photonics **4**, 535 (2010).
4. X. Sun, K. Xu, and H. X. Tang, Opt. Lett. **39**, 2514 (2014).
5. K. D. Vos, I. Bartolozzi, E. Schacht, P. Bienstman, and R. Baets, Opt. Express **15**, 7610 (2007).
6. X. Yu, H. Zhang, and X. Zheng, Opt. Commun. **267**, 83 (2006).
7. C. E. Soccolich and M. N. Islam, Opt. Lett. **14**, 645 (1989).
8. T. Y. L. Ang, S. T. Lim, S. Y. Lee, C. E. Png, and M. K. Chin, Appl. Opt. **48**, 2821 (2009).
9. D. Dai and S. He, Opt. Lett. **31**, 1988 (2006).
10. P.-H. Fu, T.-Y. Chiang, N.-C. Cheng, Y.-F. Ma, and D.-W. Huang, Appl. Opt. **55**, 3626 (2016).
11. J. Yamauchi, M. Yamanoue, and H. Nakano, J. Lightwave Technol. **26**, 1708 (2008).
12. D. Vermeulen, S. Selvaraja, P. Verheyen, P. Absil, W. Bogaerts, D. Van Thourhout, and G. Roelkens, IEEE Photon. Technol. Lett. **24**, 482 (2012).
13. M. Aamer, A. M. Gutierrez, A. Brimont, D. Vermeulen, G. Roelkens, J. M. Fedeli, A. Hakansson, and P. Sanchis, IEEE Photon. Technol. Lett. **24**, 2031 (2012).
14. S.-H. Kim, R. Takei, Y. Shoji, and T. Mizumoto, Opt. Express **17**, 11267 (2009).
15. A. V. Velasco, M. L. Calvo, P. Cheben, A. Ortega-Moñux, J. H. Schmid, C. A. Ramos, Í. M. Fernandez, J. Lapointe, M. Vachon, S. Janz, and D.-X. Xu, Opt. Lett. **37**, 365 (2012).
16. C. Brooks, P. E. Jessop, H. Deng, D. O. Yevick, and G. Tarr, Opt. Eng. **45**, 044603 (2006).
17. Y. Yue, L. Zhang, M. Song, R. G. Beausoleil, and A. E. Willner, Opt. Express **17**, 20694 (2009).
18. J. Zhang, T.-Y. Liow, M. Yu, G.-Q. Lo, and D.-L. Kwong, Opt. Express **18**, 25264 (2010).
19. H. Zhang, S. Das, J. Zhang, Y. Huang, C. Li, S. Chen, H. Zhou, M. Yu, P. G.-Q. Lo, and J. T. L. Thong, Appl. Phys. Lett. **101**, 021105 (2012).
20. Y. Ding, L. Liu, C. Peucheret, and H. Ou, Opt. Express **20**, 20021 (2012).
21. D. Dai and J. E. Bowers, Opt. Express **19**, 18614 (2011).
22. L. Liu, Y. Ding, K. Yvind, and J. M. Hvam, Opt. Lett. **36**, 1059 (2011).
23. M. Schumann, T. Buckmann, N. Gruhler, M. Wegener, and W. Pernice, Light: Sci. Appl. **3**, e175 (2014).
24. Q. Xu, L. Chen, M. G. Wood, P. Sun, and R. M. Reano, Nat. Commun. **5**, 5337 (2014).
25. Y. Yin, Z. Li, and D. Dai, J. Lightwave Technol. **35**, 2227 (2017).
26. M. Bendsoe and O. Sigmund, *Topology Optimization: Theory, Methods, and Applications* (Springer, 2013).
27. B. Shen, P. Wang, R. Polson, and R. Menon, Nat. Photonics **9**, 378 (2015).
28. A. Y. Piggott, J. Lu, K. G. Lagoudakis, J. Petykiewicz, T. M. Babinec, and J. Vučković, Nat. Photonics **9**, 374 (2015).
29. P. I. Borel, B. Bilenberg, L. H. Frandsen, T. Nielsen, J. Fage-Pedersen, A. V. Lavrinenko, J. S. Jensen, O. Sigmund, and A. Kristensen, Opt. Express **15**, 1261 (2007).
30. J. C. C. Mak, C. Sideris, J. Jeong, A. Hajimiri, and J. K. S. Poon, Opt. Lett. **41**, 3868 (2016).
31. K. Xu, L. Liu, X. Wen, W. Sun, N. Zhang, N. Yi, S. Sun, S. Xiao, and Q. Song, Opt. Lett. **42**, 855 (2017).
32. L. F. Frellsen, Y. Ding, O. Sigmund, and L. H. Frandsen, Opt. Express **24**, 16866 (2016).
33. J. Canning, N. Skivesen, M. Kristensen, L. H. Frandsen, A. Lavrinenko, C. Martelli, and A. Tetu, Opt. Express **15**, 15603 (2007).
34. L. H. Frandsen, Y. Elesin, L. F. Frellsen, M. Mitrovic, Y. Ding, O. Sigmund, and K. Yvind, Opt. Express **22**, 8525 (2014).
35. J. S. Jensen and O. Sigmund, Laser Photon. Rev. **5**, 308 (2011).
36. M. Mitchell, *An Introduction to Genetic Algorithms* (MIT, 1998).
37. https://kb.lumerical.com/en/index.html.
38. J. Wang, P. Chen, S. Chen, Y. Shi, and D. Dai, Opt. Express **22**, 12799 (2014).